



MIT Open Access Articles

Low-frequency terrestrial gravitational-wave detectors

The MIT Faculty has made this article openly available. **Please share** how this access benefits you. Your story matters.

Citation	Harms, Jan, Bram Slagmolen, Rana Adhikari, M. Miller, Matthew Evans, Yanbei Chen, Holger Müller, and Masaki Ando. "Low-Frequency Terrestrial Gravitational-Wave Detectors." Phys. Rev. D 88, no. 12 (December 2013). © 2013 American Physical Society
As Published	http://dx.doi.org/10.1103/PhysRevD.88.122003
Publisher	American Physical Society
Version	Final published version
Citable link	http://hdl.handle.net/1721.1/85093
Terms of Use	Article is made available in accordance with the publisher's policy and may be subject to US copyright law. Please refer to the publisher's site for terms of use.

Low-frequency terrestrial gravitational-wave detectors

Jan Harms,¹ Bram J.J. Slagmolen,² Rana X. Adhikari,³ M. Coleman Miller,^{4,5} Matthew Evans,⁶
Yanbei Chen,⁷ Holger Müller,⁸ and Masaki Ando^{9,10}

¹*INFN, Sezione di Firenze, Sesto Fiorentino 50019, Italy*

²*The Australian National University, Centre for Gravitational Physics, Canberra 0200, Australia*

³*LIGO Laboratory, California Institute of Technology, Division of Physics, Math, and Astronomy, Pasadena, California 91125, USA*

⁴*Department of Astronomy and Joint Space-Science Institute, University of Maryland, College Park, Maryland 20742-2421, USA*

⁵*Department of Physics and Astronomy, Johns Hopkins University, Baltimore, Maryland 21218, USA*

⁶*Kavli Institute for Astrophysics, Massachusetts Institute of Technology, Cambridge, Massachusetts 02139, USA*

⁷*California Institute of Technology, Division of Physics, Math, and Astronomy, Pasadena, California 91125, USA*

⁸*Department of Physics, University of California, Berkeley, California 94720, USA*

⁹*Department of Physics, The University of Tokyo, Tokyo 113-0033, Japan*

¹⁰*National Astronomical Observatory of Japan, Tokyo 181-8588, Japan*

(Received 12 August 2013; published 13 December 2013)

Direct detection of gravitational radiation in the audio band is being pursued with a network of kilometer-scale interferometers (LIGO, Virgo, KAGRA). Several space missions (LISA, DECIGO, BBO) have been proposed to search for sub-hertz radiation from massive astrophysical sources. Here we examine the potential sensitivity of three ground-based detector concepts aimed at radiation in the 0.1–10 Hz band. We describe the plethora of potential astrophysical sources in this band and make estimates for their event rates and thereby, the sensitivity requirements for these detectors. The scientific payoff from measuring astrophysical gravitational waves in this frequency band is great. Although we find no fundamental limits to the detector sensitivity in this band, the remaining technical limits will be extremely challenging to overcome.

DOI: [10.1103/PhysRevD.88.122003](https://doi.org/10.1103/PhysRevD.88.122003)

PACS numbers: 04.80.Nn, 95.75.Wx, 95.55.Ym, 04.30.Tv

I. INTRODUCTION

Gravitational waves (GWs) in the context of general relativity promise to reveal new information about the bulk motions of massive compact objects in the Universe. This new view of the Universe will complement our existing, electromagnetic understanding. In this decade, kilometer-scale interferometers (such as LIGO [1], Virgo [2], GEO600 [3], and KAGRA [4]) are expected to make the first direct detections of GWs in the 10–10000 Hz band [5]. These waves would be associated with the coalescence of neutron-star binaries and low-mass black-hole binaries. In the proposed underground Einstein Telescope, the approach is to improve the traditional detector design to extend the detection band down to 3 Hz [6]. A set of space interferometer missions (eLISA [7], ALIA [8], DECIGO [9], and BBO [10]) has been proposed to search for the gravitational waves from supermassive black holes as well as the inspiral phase of the low-mass compact objects [11].

The reason for constructing interferometers in space is chiefly to avoid the seismic disturbances on the Earth due to natural and anthropogenic sources. Even if we posit a very sophisticated vibration isolator, a GW detector on the Earth cannot be shielded from the fluctuations in the terrestrial gravitational forces [12,13] (aka Newtonian noise or gravity-gradient noise). In this work we argue that it is possible, with reasonable extrapolations of existing technology, to make detections of GWs in the 0.1–10 Hz using terrestrial detectors.

In Sec. II, we describe an atom interferometer with improved immunity to technical noise sources. In Sec. III, we explore improvements in a previously proposed differential torsion bar detector. In Sec. IV, we propose a version of the standard Michelson interferometer optimized for low frequency sensitivity. In Sec. V we explore options for mitigating the effects of the Newtonian gravitational noise. Finally, in Sec. VI, we explore what sources of gravitational waves can be probed using this set of terrestrial, low-frequency detectors. As will be shown, the sensitivity at 0.1 Hz to GWs should be around $10^{-20} \text{ Hz}^{-1/2}$ or better, and the corresponding instrumental designs will be referred to as MANGO in this paper.

II. ATOM INTERFEROMETERS

Atom interferometers contain a source of ultracold atoms that are released into free fall. During the fall, each atom interacts multiple times with a laser. In its simplest version, the laser-atom interactions force each atom to follow the two paths of a Mach-Zehnder type interferometer as shown in Fig. 1. The first laser-atom interaction mimics a beam splitter for the atoms, two subsequent spatially separated interactions with each partial wave packet after time T form the two mirrors of the Mach-Zehnder interferometer that recombine the two atom paths after an additional fall time T . A final atom-laser interaction at the point of recombination acts as another

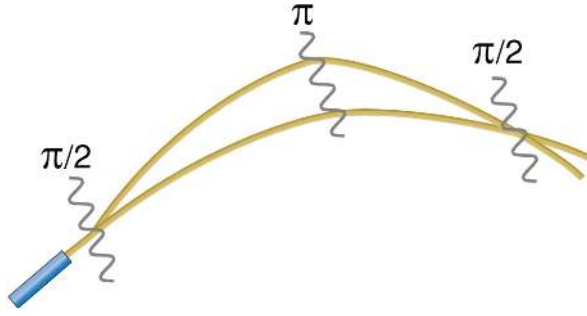


FIG. 1 (color online). Mach-Zehnder configuration of an atom interferometer. A first $\pi/2$ laser pulse splits the atom path in two. Subsequent π pulses acting as atom mirrors recombine the paths that are brought to interference by a second $\pi/2$ pulse.

atom beam splitter. The atoms can now be counted in the two output ports of the second beam splitter. In its standard implementation, two counterpropagating lasers are required at each point of interaction to induce a Doppler-sensitive two-photon transition. However, single-laser interactions have been proposed recently as a promising way to mitigate some of the dominant noise contributions [14,15].

Atom interferometers (AIs) have also been considered as a new type of GW detector. In contrast to the laser-interferometric designs such as the torsion-bar antenna and the Michelson interferometer, AIs are generally not pure gravity strain meters, but are sensitive to a multitude of field quantities including the homogeneous static gravity field, static gravity gradients, and fluctuations thereof [16]. Another interferometer topology has been proposed that combines the benefits of freely falling atoms and long-baseline laser interferometry [17,18]. In these schemes, two or more AIs interact with the same lasers. In this type of configuration, the AI itself no longer serves as a GW detector, but each AI constitutes a *freely falling phase meter* for the lasers. Since the atoms are freely falling, these detectors are less sensitive to seismic perturbations, which is one of the major disturbances in conventional laser-interferometric detectors, requiring sophisticated vibration isolation engineering [19,20].

As reported previously [21], seismic noise is still relevant in laser-atom interferometers (LAIs), but it is strongly suppressed compared to seismic noise in standard laser-interferometric GW detectors. This is because any type of laser noise measured differentially between two freely falling phase meters (atom interferometers) is subject to a common-mode rejection to leading order, but does enter at order $\Omega L/c$, where c is the speed of light, L is the distance between the two atom interferometers, and Ω is the signal frequency. Therefore, compared to conventional laser-interferometric detectors, the advantage of atom interferometers is that the common-mode rejection of seismic displacement is established optically rather than by seismic correlations between test masses. However, the

results also show that laser-frequency noise needs to be further suppressed interferometrically; otherwise laser-frequency noise would pose a strong limit on the sensitivity of these detectors. Interestingly, this is ultimately a consequence of the fact that two counterpropagating lasers have to interact simultaneously with each atom. As discussed in [14,15], atom GW detectors based on atom interactions with a single laser could ideally be free of laser-frequency noise (including the seismic noise) even without a laser interferometer. In the latter case, the detector could be built along a single baseline, which would be a great advantage for underground atom GW detectors since they could be constructed with a vertical baseline and vertically falling atoms. In contrast, the phase signal of each atom interferometer is first-order insensitive to the initial positions and velocities of the atoms, but constraints on the distribution of atom trajectories need to be fulfilled for example to sufficiently suppress noise associated with wave-front aberrations [22].

The main noise contributions of atom interferometers that have been described in previous publications are the atom shot noise, the laser-frequency noise, Newtonian noise (see Section V), and noise associated with laser wave-front aberrations [22,23]. In the following, we will base our noise model on a standard LAI configuration with two perpendicular horizontal baselines of length 500 m to suppress laser-frequency noise electronically similar to the time-delay interferometers envisioned for space-borne GW detectors such as eLISA [24]. Seismic isolation systems are required for the main laser optics shown in Fig. 2 and for auxiliary optics forming the spatial mode filter of the input beam, but since none of the optics serves as the test mass, the isolation requirements are less stringent.

With respect to the laser-frequency noise published in [25], an additional suppression of 10^5 is assumed for the noise curve in Fig. 3. Most of this suppression (10^3) will be

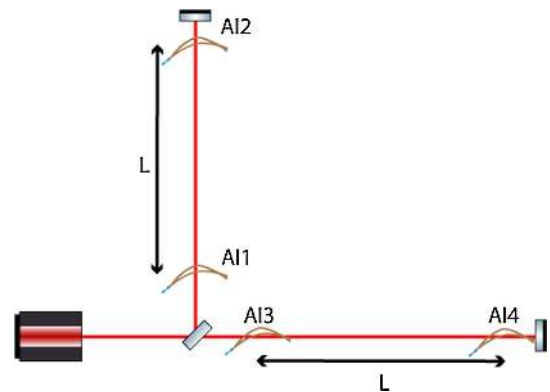


FIG. 2 (color online). Sketch of a possible GW detector that combines atom and laser interferometry. Each of two pairs of atom interferometers (AI) measure the differential phase of the laser at a distance L from each other. These two differential phase signals are further subtracted from each other to cancel the laser phase noise.

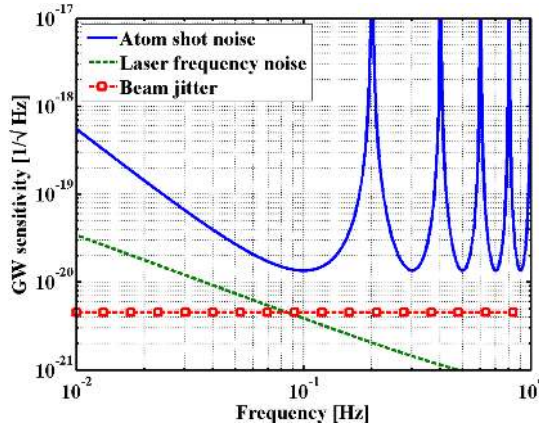


FIG. 3 (color online). Sensitivity curve of the MANGO concept for a laser-atom interferometer based on the parameter values given in Table I. The noise peaks are a consequence of the transfer function between laser and atom phases, and are characteristic for the Mach-Zehnder configuration of the atom interferometers.

achieved by performing a differential readout between the two arms of the Michelson interferometer. However, since asymmetries between the two arms can impede noise suppression, it seems likely that MANGO sensitivity can only be achieved with an additional $100\times$ improvement in laser frequency stabilization in the 0.1–10 Hz band relative to the level published in [25]. This should be possible using the new generation of cryogenic laser reference cavities with crystalline mirror coatings [26], or building on recent progress with superradiant lasers [27]. Random displacement of the laser optics can produce excess laser-frequency noise as well as laser beam jitter that converts into atom phase noise. With respect to excess frequency noise, the requirements for seismic noise reduction around 0.1 Hz can be about 6 orders of magnitude less stringent than they are for suspended test masses. The isolation chain up to the suspension-point interferometer (SPI) stage presented in Sec. IV without the optical-rigid-body (ORB) and final suspension stage would provide sufficient seismic-noise suppression in the longitudinal degree of freedom (see below for additional requirements with respect to rotational degrees of freedom). The residual seismic noise $\Omega\xi/c$ (ξ the optics displacement noise, Ω the signal frequency) is less than $10^{-22}/\sqrt{\text{Hz}}$ at 0.1 Hz. In this configuration the optics cannot be considered free, and also the distance between laser optics is controlled over the entire detection band; consequently, the optical response to GWs is suppressed. Hence, sensitivity estimates can be obtained just by considering the distance change between pairs of atom interferometers.

Static wave-front aberrations contribute to the instrumental noise if the laser beam jitters due to the random tilt of the optics or the laser [22,23]. To provide the required alignment stability of the laser beams relative to the atoms, one first needs a stable reference, which consists of

seismically isolated optics and components of the alignment control system. Then the beam jitter can be suppressed relative to Ref. [28]. Also the static wave-front aberrations can be reduced by mode cleaning [29], ultimately being limited by aberrations of the optics. Extrapolating current optics polishing and coating quality, we assume that static wave-front aberrations of 10^{-4} rad should be possible. The beam jitter noise curve in Fig. 3 was plotted with a beam jitter of 10^{-11} rad/ $\sqrt{\text{Hz}}$ at 0.1 Hz; for comparison, this is $\sim 100\times$ better than the best angular stabilization achieved with the LIGO interferometers using differential radio frequency wave-front sensing. Even though it seems feasible to build a control system that can suppress beam jitter down to this level, it will be very challenging to provide the seismic isolation with respect to tilt/yaw motion. This can only be achieved through passive seismic isolation or by implementing other inertial references. A solution would be to implement a multistage passive isolation further reducing seismic noise in all degrees of freedom. Additional suppression of beam jitter noise can be achieved by implementing adaptive optics to correct wave-front aberrations.

In addition to static wave-front aberrations that convert into atom-phase noise through beam jitter, dynamic wave-front aberrations generated by Brownian noise in the optics coatings cause additional atom phase noise. As for the beam jitter case, noise from small-scale aberrations is strongly suppressed [23], and we can focus on the largest scale aberration for the noise estimate, which corresponds to a spatial wavelength equal to half of the beam diameter. In this case, assuming a mirror at room temperature with a coating quality factor $Q = 10^4$, the atom phase noise at 0.1 Hz in units of GW strain is less than $10^{-24}/\sqrt{\text{Hz}}$.

Besides Newtonian noise, the most significant noise contribution is the atom shot noise governed by the flux η of cold atoms interacting with the laser beams, and the number n of photons transferred to each atom at each point of interaction with the lasers, which determines the momentum transfer from light to atoms. Since the standard-quantum limit enforces a strong limit on the photon number in low-frequency laser-interferometric detectors, it seems feasible that atom shot noise can be brought to a level comparable to photon shot noise. Atom shot noise is proportional to $1/n$ and $1/\sqrt{\eta}$. The parameter values used for the noise curve in Fig. 3 are $\eta = 10^{14}$ atoms/s (about a factor 10^6 above current state-of-the-art [30]) for the atom throughput and $n = 1000$ for the number of photons (about a factor of 10 above current state-of-the-art [31]). Momentum transfers with $n = 102$ photons have already been realized but without being able to measure phases [32]. As outlined in [18], an ambitious but straightforward R&D effort could lead to an atom flux as high as 10^{14} atoms/s by increasing laser power for a two-dimensional magneto-optical trap. Another option to mitigate atom shot noise is to prepare the atoms in phase-squeezed

states through nonlinear atom interactions, but atom phase-squeezing has not been demonstrated yet in atom interferometers.

In summary, major technology advances and better understanding of noise sources in LAIs are required to achieve the sensitivity goal. Such insight can only be obtained through further theoretical studies, and eventually through prototyping of detectors. An important first step toward low-frequency GW detection would be to achieve sensitivities that would allow us to observe terrestrial gravity perturbations around 0.1 Hz and to demonstrate Newtonian-noise subtraction at these frequencies. From Sec. V we know that this can already be achieved with strain sensitivities around $10^{-16}/\sqrt{\text{Hz}}$ (more easily in environments with elevated seismic and infrasound noise). This sensitivity could be achieved with a single baseline LAI using state-of-the-art laser-frequency stabilization [25]. Moreover, only modest seismic-noise suppression by about a factor of 1000 to avoid excess laser-frequency noise (about 10 orders of magnitude are required for Advanced Virgo and LIGO above 10 Hz) and a modest increase of momentum transfer to $n = 100$ are sufficient, while using already available atom flux. The length of the baseline would still have to be around 500 m, which can be made smaller if either η or n are further increased.

III. THE TORSION BAR ANTENNA

A torsion-bar antenna (TOBA) is a new type of gravitational wave detector [33]. The tidal-force fluctuations caused by GWs are observed as differential rotations between two orthogonal bars, independently suspended as torsion pendulums. They share the same suspension point, have their axis of rotation colinear and center-of-mass coincident. This is a crucial design feature and will provide a high level common mode rejection (~ 1 part in 1000) from mechanical noise. Shown in Fig. 4, an incoming gravitational wave, incident into the page, will rotate the

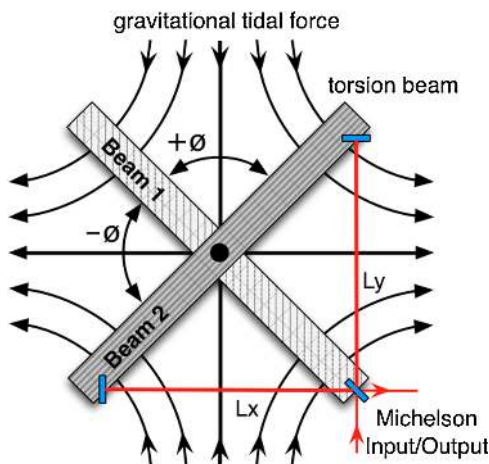


FIG. 4 (color online). Interaction of TOBA's dual torsion beam configuration with GW tidal forces.

beams differentially. The linear distance between the ends of the beams, L_x and L_y , will change. The differential length changes will be measured in the same way as in the long baseline gravitational wave detector (LIGO, VIRGO). Any linear pendulum motion between the beams will be registered as a common mode motion, to which the Michelson is insensitive.

A. The torsion pendulum

The anticipated design for a large-scale TOBA detector has a suspended mass of $\sim 10^4$ kg (10 m long \times 0.6 m diameter), made from a high quality low-loss material compatible with cryogenics like silicon or aluminium 5056. The aspect ratio of the bar is optimized to maximize the eigenfrequency of the second bending mode, to be above 10 Hz, which generates a differential displacement between the two ends. The torsion wires need to be made from a similar high quality factor material. The fundamental torsion frequency will be around 30 μHz . Increasing the length of the bar will improve the overall sensitivity, yet it will also increase the thermal noise associated with its internal modes. Constructing the bar with a dumbbell shape is another possibility to increase the bar's inertia by a factor of 3. The detector will operate at cryogenic temperatures to mitigate the thermal noise (suspension thermal noise in particular).

One of the challenges is to mount the two bars such that there is no cross coupling between the torsional and other modes. One approach is to drill a hole in the middle of one bar, while narrowing the center of the other bar. Other mechanical configurations are under investigation, such as adjusting the height of the suspension points on the bar, while maintaining the location of the center of mass. Figure 5 shows a complete schematics overview of the TOBA suspension design. Here the two bars are illustrated as solid beams.

As an alternative to solid bars, the bars can be made of a light open frame structure with large masses at the ends. This will be detrimental for the thermal noise (and low eigenmode frequencies); however, linear cavities along the length of the structure can monitor the modal displacements between the end masses. A feedback system using inertial actuators (e.g., mass on a piezoelectric actuator) located at the antinodes of the first few structural modes can be used to damp the eigenmodes. Alternatively, recorded modal displacement can be used in postprocessing cancellation schemes.

The torsion bars are suspended from a common suspension point (TOBA Suspension Point in Fig. 5), improving the common mode rejection. The two bars have two suspension wires to accommodate the coincidence of their axis of rotation. The wires will have a small separation at the suspension point and at the bar. The impact on the torsion frequency will be modest if the suspension wires are sufficiently long.

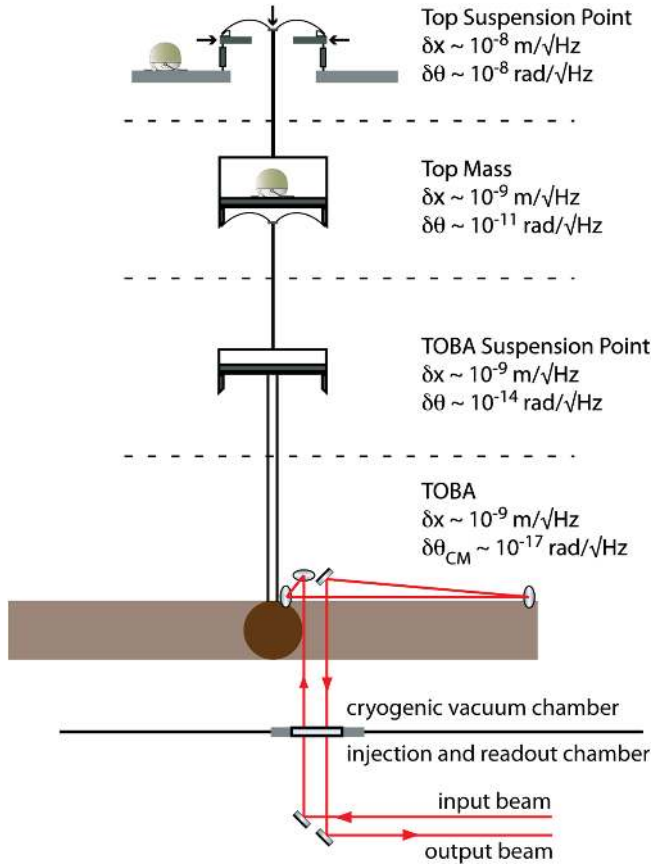


FIG. 5 (color online). Schematic overview of the TOBA suspension design, with the horizontal bar at the bottom and the second bar indicated with the darker circle coming out of the page.

B. Isolation chain

The TOBA Suspension Point is suspended from a two stage isolation chain, inside a vacuum chamber to reduce seismic and acoustic coupling (see Fig. 5). The base of the Top Suspension Point is mounted to the ground. The Top Suspension Point is isolated in 4 degrees of freedom (no roll or pitch DOF), via an inverted pendulum and a geometric antispring filter [34]. It has actuators for each degree of freedom with respect to the ground. To reduce the force actuation it is desirable to have the eigenmodes up to 500 mHz.

The Top Mass in Fig. 5 is suspended from the Top Suspension Point via a single wire and is used as a reference to stabilize the residual seismic motion. A high-sensitivity broadband seismometer is mounted inside the Top Mass and registers any residual motion. The sensor data are used in a feedback control system to the actuators at the Top Suspension Point. The seismometer is housed in a pod to make it vacuum compatible, shielded from magnetic field noise and temperature stabilized to improve noise performance at low frequencies ($< 1 \text{ Hz}$). The actuators will suppress the motion of the top mass down to the noise floor of the seismometer ($\approx 10^{-9} \text{ m}/\sqrt{\text{Hz}}$ [35]).

The TOBA Suspension Point is suspended from the Top Mass via a suspension wire and vertical blades, providing an additional 6 degrees of isolation. This acts as a reference for the various sensors and actuators to the individual bars.

To reduce the suspension thermal noise, the TOBA Suspension Point and below is cooled down to 4 K. The whole suspension chain will be wrapped in a heat shield to maintain the cryogenic temperatures.

C. Interferometric readout

The differential rotation between the two bars is obtained by measuring the distance fluctuation between the ends of the two bars. With respect to the first bar, the ends of the second bar will advance and retreat when the bars rotate (differentially). A Michelson interferometer, with the beam splitter on the first bar and end mirrors on the second bar, is used to measure the change in length, shown in Fig. 4.

To reduce the effect of the mirror coating thermal noise on the readout, large beam sizes on mirrors is beneficial. The optical input and output beams for the Michelson come from underneath the bars, with the injection and readout optics, such as the recycling cavities, in a separate chamber. This greatly simplifies the optical configuration on the bars and will separate the more complex optical readout from the mechanical system. The final readout will be done using the direct current (DC) readout technique [36] with a possible implementation of quantum-nondemolition techniques for broadband improvement of the shot noise.

Figure 6 shows an anticipated sensitivity of a TOBA detector, operating at 4 K. The seismic noise is set to the instrumental noise level of a broadband seismometer, $5 \times 10^{-10} \text{ m}/\sqrt{\text{Hz}}$ at 0.1 Hz, followed by a second pendulum

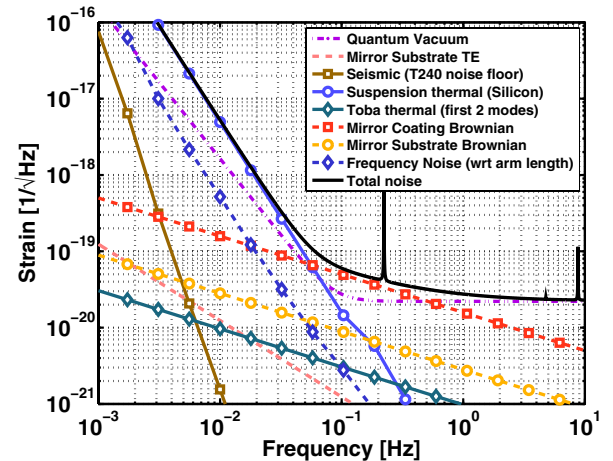


FIG. 6 (color online). Noise plot of the MANGO concept for a torsion detector with 10 m long by 0.5 m diameter fused silica bars (7560 kg each) operated at 4 K. Each bar is suspended by two 5 m long and 2.6 mm diameter silicon wires. The input power is set to 10 W with no recycling cavities and a finesse of the arm cavities 313.

stage and a 1:1000 coupling from horizontal to rotation. An estimate of the force sensitivity of the large-scale TOBA can be approximated with $\tau = I\alpha = -I\theta\omega^2 = -I(\delta x/l)(2\pi f)^2$. With a modeled design sensitivity of $10^{-19} \text{ m}/\sqrt{\text{Hz}}$ at 1 Hz, the torque is then $97 \times 10^3 \times (10^{-18}/10)(2\pi \times 10^{-3})^2 = 4 \times 10^{-17} \text{ Nm}/\sqrt{\text{Hz}}$. At the end of the 10 m bar a linear force as small as $\sim 10^{-17} \text{ N}/\sqrt{\text{Hz}}$ can be measured.

The TOBA concept is less constrained by fundamental noise sources, but it would certainly require outstanding engineering achievements to realize this MANGO concept, such as fabricating a high-Q bar of length 10 m or longer cooled to a temperature of 4 K. Though such a cryogenic system is well established in resonant-bar GW detectors [37], about a factor of 3 enlargement is required for this TOBA design.

IV. MICHELSON INTERFEROMETER

Another approach to low frequency ground-based gravitational-wave detection is to modify the existing laser interferometric detector design. These detectors are limited at low frequencies by seismic noise, thermal noise, and radiation pressure noise. Though ground-based detectors all have extensive seismic isolation systems, seismic noise is dominant below ~ 5 Hz. As we describe below, an extension of the suspension point interferometer [38,39] concept to many degrees of freedom can potentially provide significant rejection of seismic noise coupling.

To best make an ORB with interferometric sensing, a triangular configuration is chosen over the L-shape in use today. This provides high sensitivity to all motions in the plane of the interferometer, making the horizontal “stiffness” of the ORB as high as possible. This configuration also has other advantages as a GW detector, as discussed in various proposals for future detectors (ET, LISA, BBO), including redundancy and sensitivity to both GW polarizations.

A. Preisolation

The first stages of seismic isolation for the Michelson interferometer are similar to those currently in use in ground-based GW detectors (e.g., Advanced LIGO). An active preisolation stage reduces somewhat the noise transmitted to lower stages, and provides a wide range actuator for positioning the suspension chain.

A second layer of isolation is provided by low-frequency passive mechanical resonators (e.g., Robert’s linkages for horizontal and Euler buckling springs for vertical [40,41]). These can be tuned to a few megahertz to provide modest in-band isolation and significant reduction of the microseism at 100 mHz.

The target for preisolation is to arrive at $1 \text{ nm}/\sqrt{\text{Hz}}$ at 10 mHz, and $100 \text{ pm}/\sqrt{\text{Hz}}$ above 100 mHz. This motion is assumed to be present in all translational degrees of freedom and incoherent between platforms.

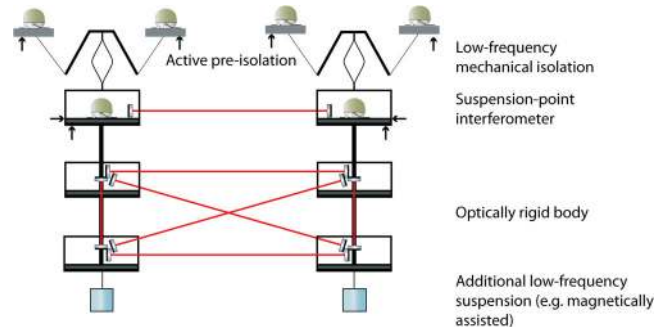


FIG. 7 (color online). Seismic isolation for the Michelson low-frequency detector is provided by a multi-stage suspension with interferometric length and angle sensing.

B. Suspension point interferometer

The next layer (cf. Fig. 7) of isolation links the three detector platforms with Fabry-Perot cavities in a configuration known as the SPI. The SPI layer serves to reduce the relative motion of the three platforms in the plane of the interferometer and to provide interferometric alignment signals for the platforms. In total, the SPI produces three displacement signals and nine alignment signals, while the three platforms have a total of 18 rigid-body degrees of freedom (DOFs). Thus, the available signals are sufficient to constrain the three platforms to behave as a single rigid body, by removing 12 internal DOFs and leaving 6 DOFs uncontrolled (the SPI is clearly insensitive to translation and rotation of the three platforms as a rigid body).

The alignment signals that provide the majority of the constraints, when coupled with small lever arms, have a sensitivity comparable to the displacement signals produced when the platforms are displaced in the plane. That is, if we consider an SPI made of low-finesse cavities with a few 100 mW of stored power, a 1 mm lever arm makes the $10^{-13} \text{ rad}/\sqrt{\text{Hz}}$ sensitivity of a wave-front sensor comparable to the $10^{-16} \text{ m}/\sqrt{\text{Hz}}$ shot noise limited displacement sensitivity.

The differential vertical motion (DVM) of the platforms, however, is a different matter. DVM is detected by the SPI only through angular signals and has an effective lever arm of the distance between the platforms (e.g., several hundred meters). Designing the SPI cavities to be nearly concentric, with the radii of curvature of the mirrors slightly larger than half the length of the cavity, can increase their sensitivity to DVM by a factor of 10 or even 100. This displacement noise will, however, remain 3 to 4 orders of magnitude larger than the in-plane displacement noises, and only marginally lower than the noise level provided by the preisolators.

The net effect is that common motion of the three platforms, and their differential vertical motion, remain at or near the noise level given by the preisolators. These

noises will couple into later stages of the isolation chain via small asymmetries in the suspensions to produce motion in the plane of the interferometer. A well tuned mechanical system can minimize these couplings, possibly to less than 10^{-4} with *in situ* tuning, limited by thermally driven mechanical drifts in the suspension system. The existence of these cross couplings is the reason that a single layer SPI is not sufficient to bridge the 8 orders of magnitude gap between the preisolator output noise and the noise level required at the test-mass suspension stage.

Since greater suppression would most likely be futile, the SPI stage aims to reduce the relative motion of the platforms to 10^{-14} m/ $\sqrt{\text{Hz}}$ at 100 mHz, or 10^{-4} times the noise floor presented by the preisolator. If significantly better decoupling is available, the relative motion can in principle be further reduced to approach the shot noise level of the SPI around 10^{-16} m/ $\sqrt{\text{Hz}}$.

C. Optical rigid body

The final layer of seismic isolation in the interferometer suspension chain is the optical rigid body; essentially a multicavity SPI that is designed to *maximize* the coupling of vertical displacement to the readout. The collection of resonant optical cavities that constitute the ORB are arranged such that any differential displacement of the platforms appears as a longitudinal displacement of at least one cavity. When all of these cavities are held at their resonance points with active control loops, the three independently suspended platforms are forced to move as a rigid body. Furthermore, since the ORB cavities span mechanically separated layers in the suspension chain, the bottom layer can be used as a proof mass in an “interferometric seismometer,” thereby allowing for the reduction of common motion of the ORB.

The aim of the ORB is to reduce the common displacement, and differential vertical motion, to 10^{-13} m/ $\sqrt{\text{Hz}}$ at 100 mHz at the bottom layer of the suspension chain. The in-plane differential motion can then be reduced to the shot noise level of the bottom layer ORB cavities around 10^{-16} m/ $\sqrt{\text{Hz}}$. These are the noise levels presented as inputs to the final suspension stage that holds the interferometer test masses.

It is worth noting that the ORB is in principle sensitive to gravitational waves, since it is made of optical cavities identical to the ones used in the test-mass stage interferometer. Since the ORB control loops suppress any detected motion of the suspended platforms, they will also suppress any GW signal that appears within its control bandwidth. Thus, below the resonance frequency of the final-test mass suspension stage, the interferometer that hangs from the ORB will be insensitive to GWs. Above that frequency, however, the test masses are free to move relative to the ORB and the GW signal is not suppressed. Since the resonance of the test-mass suspension is necessarily below

the GW detection band, suppression of the GW signal by the ORB is not a problem.

D. Magnetomechanical suspension

The final suspension stage of this low frequency Michelson interferometer presents several technical challenges. The most obvious of these is to attain a pendular resonance frequency below the band of interest for GW detection; in our case this is 10 mHz.

The second major challenge of the final suspension stage is to provide low thermal noise. The thermal noise of a simple pendulum suspension, above the mechanical resonance, is given by

$$x_{\text{thermal}} = \frac{1}{m\omega^2} \sqrt{\frac{4k_B T k \phi}{\omega}} = \sqrt{\frac{4k_B T \omega_0^2}{mQ\omega^5}}, \quad (1)$$

where $k_B T$ is the Boltzman constant times the suspension temperature, m the suspended mass, k the effective spring constant, $Q = 1/\phi$ the quality factor and ϕ the loss angle of the restoring spring, $\omega_0 = \sqrt{k/m}$ the resonant frequency, and ω the measurement frequency. To put in some rough numbers, a 1 mHz suspension with $Q = 10^8$ holding a 100 kg test mass would result in $\sim 3 \times 10^{-17}$ m/ $\sqrt{\text{Hz}}$ thermal noise at 100 mHz; this is not enough to reach the MANGO goal.

In a magnetic or magnetically assisted suspension [42–44], the thermal noise may come not only from the restoring force of the suspension but also from the deformation of the suspension element that counters the force of gravity. Magnetic suspensions may also have losses due to magnetostriction in the support magnets and eddy current damping in conductive suspension components. It may be possible to avoid some of these issues by using an electrostatic suspension instead [45].

The third major challenge is matching; the common motion of the ORB can become differential motion of the test masses if the restoring forces of the test-mass suspensions are not perfectly matched. Numerically speaking, the suspensions must be matched well enough to reject the 10^{-13} m/ $\sqrt{\text{Hz}}$ common motion of the ORB at a level of $\sim 10^5$ to prevent it from spoiling the detector sensitivity.

E. Detector sensitivity

To reach a strain noise level of less than 10^{-20} / $\sqrt{\text{Hz}}$ at 0.1 Hz, major developments in suspension and quantum-noise technology are required. The parameter values for the Michelson MANGO configuration are summarized in Table I. The quantum noise is achieved by applying quantum-nondemolition (QND) techniques [46] such as a speed-meter design. However, these can only be realized by means of extreme low-loss, small-bandwidth (i.e. ~ 0.1 Hz) optical resonators, or alternatively, phenomena in light-atom interactions such as electromagnetically induced transparency [47,48] could potentially fulfill

TABLE I. Interferometer parameters used for the MANGO detectors.

Parameter	Symbol	Value	Units	Parameter	Symbol	Value	Units
Michelson interferometer							
Light wavelength	λ	1550	nm	Substrate Young's modulus	Y_{sub}	185	GPa
Mirror mass	m	600	kg	Suspension temperature	T_{sus}	0.2	K
Arm cavity length	L	300	m	Suspension ribbon	\cdots	Silicon	\cdots
Arm cavity power	P_{cav}	50	W	Substrate loss angle	ϕ_{sub}	3×10^{-9}	rad
Beam radius	ω	1	cm	Coating loss angle	ϕ_{coat}	2×10^{-5}	rad
Detection efficiency	η	0.95	\cdots	Mirror coating	\cdots	GaAs:AlAs	\cdots
Squeeze factor	R	10	dB	Mirror temperature	T	120	K
Torsion-bar antenna							
Power	P	10	W	Torsion resonance frequency	ω_{tor}	0.2	mHz
Mirror substrate	\cdots	Silicon	\cdots	Bar length	L_{bar}	10	m
Beam radius	ω	2	mm	Bar diameter	d	0.5	m
Bar substrate	\cdots	Fused silica	\cdots	Suspension temperature	T_{sus}	4	K
Suspension wire	\cdots	Silicon	\cdots	Bar temperature	T_{bar}	4	K
Suspension length	L_{sus}	5	m				
Laser-atom interferometer							
Arm length	L	500	m	Coating loss angle	ϕ_{coat}	10^{-4}	rad
Momentum transfer	n	1000	\cdots	Wave-front aberrations	$\delta\phi_{\text{wf}}$	10^{-4}	rad
Atom throughput	η	10^{14}	s^{-1}	Beam jitter	$\delta\alpha$	10^{-11}	$\text{rad}/\text{Hz}^{1/2}$
Beam radius	ω	1.5	cm				

the same purpose. A less ambitious detector design would not rely on QND techniques. Reducing the mirror mass to 90 kg, and optimizing the laser power, a strain sensitivity can be achieved that is about a factor 10 smaller above 0.1 Hz and is shown in Fig. 8 as “MANGO w/o QND.”

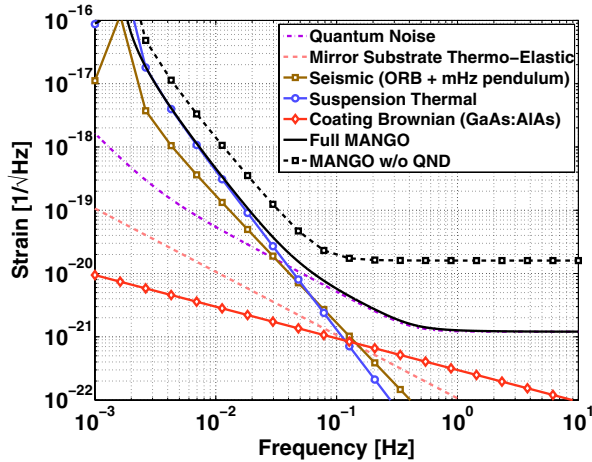


FIG. 8 (color online). Strain noise of the MANGO concept for the dual-recycled, Fabry-Perot Michelson interferometer with 300 m arms, and a speed-meter cavity used to suppress the radiation pressure noise. All fundamental noise contributors are included. This noise budget is intended to represent the best sensitivity currently imaginable. For comparison, the sensitivity is also shown for a less ambitious design with respect to radiation-pressure noise reduction.

V. NEWTONIAN NOISE

One of the foremost problems of ground-based GW detectors operating at frequencies below 10 Hz and common to all detector types is the Newtonian noise (NN). Newtonian noise is generated by a fluctuating terrestrial gravity field. In the following, we will discuss some of the known contributions to NN, and we conclude with a brief review of coherent NN subtraction.

It should be noted that atom interferometers can have additional Newtonian noise terms compared to laser-interferometric GW detectors [16,49] since the phase evolution of matter waves depends on the gravity potential. These terms add to the NN response from distance changes between two atom interferometers. However, at least for the LAI configuration discussed in Sec. II based on Mach-Zehnder atom interferometers, one finds that the total NN in units of GW strain is identical to NN in laser-interferometric GW detectors (if this was not so, then NN could be coherently subtracted from a LAI using data from a collocated, equally long laser-interferometric GW detector, and vice versa).

A. Seismic and atmospheric NN

The two main contributions to NN are produced by the ambient seismic field [12,13,50] and density fluctuations in the atmosphere [51]. Even though the main focus of these publications is to provide NN estimates for the LIGO and Virgo detectors, it is possible to extend the models to lower frequencies.

To obtain an accurate model of seismic NN, one needs detailed information about the seismic field. In some sense, seismic NN estimation below 1 Hz is easier since the properties of the seismic field do not depend significantly on detector depth, and also the seismic field can often be understood by studying data from large-scale seismic networks operated by seismologists without the necessity to carry out additional site studies. Whereas body waves can dominate the seismic field at higher frequencies especially at underground or remote sites, the dominant contribution below a few tens of a hertz is almost always the Rayleigh-wave field, which is consistent with our understanding of seismic sources being mostly located at the surface (or at shallow depths relative to the length of Rayleigh waves) [52]. Therefore, the NN estimate presented here will be derived from the Rayleigh-wave field. The equation for the gravity perturbation of a single test mass at height h above ground by a plane Rayleigh wave is given by

$$x(\Omega) = -2\pi i \cos(\theta) G \rho_0 \gamma_R \xi_z(\Omega) / \Omega^2 \exp(-\Omega h / c_R), \quad (2)$$

where $\xi_z(\Omega)$ is the vertical displacement amplitude measured at the surface directly beneath the test mass, $\gamma_R \approx 0.83$ is a material dependent factor that accounts for the partial cancellation of NN from surface displacement due to the subsurface compressional wave content of the Rayleigh-wave field, $c_R \approx 3.5$ km/s is the speed of Rayleigh waves, θ is the angle between the horizontal direction x along which the test-mass displacement is calculated and the direction of propagation of the Rayleigh wave, ρ_0 is the mean mass density of the ground, and G is Newton's gravitational constant. At low frequencies the exponential term is approximately equal to 1, and the gravity perturbation does not depend explicitly on the Rayleigh-wave speed anymore. In this case the same equation can also be used as an approximation for underground gravity perturbations. The exact expression for underground gravity perturbations from Rayleigh waves as should be used for underground detectors at a shallow depth operating at higher frequencies is more complex and involves details about the geometry of the cavity that hosts the detector. An expression similar to equation (2) is obtained for gravity perturbations along the vertical direction (without the $\pi/2$ phase shift). Finally, the factor γ_R would have a different value for Rayleigh overtones [13]. Here we will assume that the dominant waves are fundamental Rayleigh waves.

In contrast to the advanced detectors that will sense gravity perturbations as differential displacement noise that is uncorrelated between the test masses, terrestrial low-frequency detectors will sense gravity gradients since the length L of the detector arms is much smaller than the length of a seismic wave. Therefore, $\Omega L / c_R \ll 1$, and the gravity gradient perturbation along the horizontal direction x is obtained by multiplying Eq. (2) with $\cos(\theta) i \Omega L / c_R$.

It follows that the Newtonian strain noise x/L (legitimately deserving the name gravity-gradient noise at low frequencies) is independent of the arm length.

Creighton [51] describes several types of atmospheric NN. In this paper we will focus on gravity perturbations produced by infrasound waves. It is not obvious that infrasound NN is the dominant contribution since there are no accurate models for most atmospheric gravity perturbations at low frequencies. However, extending the Creighton models naively to lower frequencies and assuming that the detectors are located sufficiently far underground, other contributions to the atmospheric NN become insignificant since their noise spectral densities fall rapidly with increasing distance to the test masses. Infrasound waves are the analog of compressional seismic body waves propagating in media with vanishing shear modulus. As for the seismic NN, we first calculate the gravity perturbation from a single plane infrasound wave. The density perturbation of an infrasound wave can be written as

$$\delta \rho = \frac{\rho_0}{\gamma} \frac{\delta p}{p_0}, \quad (3)$$

where γ is the adiabatic coefficient of air, and ρ_0 is the mean air density. The relative pressure fluctuations $\delta p / p_0$ can be taken from published measurements [53]. The infrasound wave is incident on the Earth's surface at an angle θ with respect to the normal of the surface and is reflected from it without energy loss. Then the horizontal gravity perturbation at a depth z_0 reads

$$x(\Omega) = -4\pi i \sin(\theta) \cos(\phi) G \delta \rho c_{IS} \times \exp(\sin(\theta) \Omega z_0 / c_{IS}) / \Omega^3 \quad (4)$$

with $z_0 \leq 0$, c_{IS} is the speed of the infrasound wave, and ϕ is the angle between the horizontal component of the propagation direction and the direction of test-mass displacement x . As for seismic NN, the low-frequency infrasound strain noise is independent of the arm length of the detector.

The reduction of infrasound NN with depths depends on the angle of incidence. Similar to the case of Rayleigh waves, it is the apparent horizontal wavelength that determines the exponential reduction. Infrasound waves that propagate nearly horizontally produce gravity perturbations that have a large projection onto the horizontal direction x , but the gravity perturbation falls rapidly with depth. Gravity perturbations from infrasound waves that travel almost vertically cannot be efficiently reduced by going underground, but they also have a very small projection onto the direction x . This feature needs to be investigated more carefully in the future since it is well known that the infrasound field is highly anisotropic at lower frequencies [54]. However, it should be clear that for realizable detector depths the exponential reduction will not be very significant in general. Before we present the noise curves for the seismic and infrasound NN, we summarize the underlying simplifications.

Seismic Newtonian noise

- (i) *Integration is carried out over the seismic field in a half space.* Newtonian noise at the lowest frequencies may depend on the Earth's curvature.
- (ii) *The field is dominated by fundamental Rayleigh waves.* Especially with respect to NN mitigation, one needs to consider possible contributions from body waves and Rayleigh overtones.
- (iii) *Effects of underground cavities on NN are neglected.* Underground detectors in cavities may also be sensitive to gravity perturbations from shear waves [55]. Seismic NN in underground detectors depends on the geometry of the cavity, and scattered waves contribute to NN. The latter two effects should be negligible at low frequencies.
- (iv) *Rayleigh waves have frequency-independent speed.* In reality, Rayleigh waves can show strong dispersion [56] also below 1 Hz. The speed of continental Rayleigh waves lies within 2–4 km/s between 10 mHz and 1 Hz. However, since seismic NN at low frequencies does not depend significantly on the speed of seismic waves, implementing a realistic dispersion should not alter the results very much.
- (v) *Propagation-direction averaged NN is calculated assuming an isotropic seismic field.* It is well known that the seismic field can show significant anisotropies especially at low frequencies [57].

Infrasound Newtonian noise

- (i) *Integration is carried out over the infrasound field in a half-space.* The thickness of the atmosphere can be a fraction of the length of infrasound waves. For this reason it should be expected that infrasound NN is significantly smaller below 0.1 Hz than reported in this paper. In addition, infrasound waves are reflected from layers of the atmosphere (i.e. the stratosphere or thermosphere) at characteristic angles [54]. Newtonian noise at lowest frequencies may depend on the Earth's curvature.
- (ii) *Mean air density, air pressure, and speed of infrasound waves do not change with altitude.*
- (iii) *The speed of sound is frequency independent.* There are no studies of the dispersion of atmospheric infrasound at low frequencies (especially as a function of altitude). For a given infrasound field, dispersion has a weak effect on NN below 1 Hz.
- (iv) *The atmosphere does not move.* Winds play an important role in the propagation of infrasound leading to characteristic patterns in the field [54]. It is unclear if wind in relation to infrasound waves has additional consequences for NN apart from the fact that wind can be a local source of infrasound when interacting with surface structure.
- (v) *Propagation-direction averaged NN is calculated for an isotropic infrasound field.* Isotropy is certainly an unrealistic assumption as mentioned before.

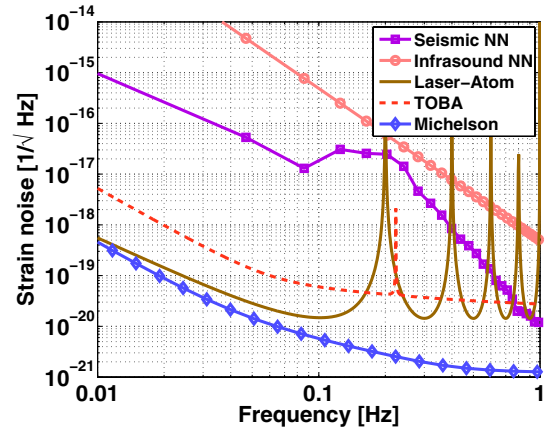


FIG. 9 (color online). Seismic Rayleigh wave and atmospheric infrasound NN together with the sensitivity curves of the three MANGO concepts.

Using the seismic spectrum published in [58] and a fit to the pressure spectrum published in [53], we obtain the NN curves presented in Fig. 9. As a final remark we want to point out that both seismic and infrasound NN have lower limits since seismic and infrasound spectra both lie above global low-noise models [59,60]. Therefore, in terms of site selection, the goal should be to identify a site where both spectra are close to the respective low-noise models.

B. Gravity transients

The GW community has not paid much attention to terrestrial gravity transients in the past except for a paper on anthropogenic noise focusing on surface detectors such as LIGO or Virgo [61]. The reason for this is that gravity transients can be eliminated in high-frequency detectors simply by avoiding abrupt changes in the velocity of moving objects and humans within a zone of about 10 m radius around the test masses. The situation is very different for low-frequency detectors. Even though the terrestrial transient landscape is completely unknown and difficult to model in many cases, it is possible to identify potentially significant contributions.

a. Newtonian noise from uniformly moving objects.— We consider the case of an object that is moving at constant speed v along a straight line that has distance r_j to a test mass at the closest approach. Therefore, the vector \vec{r}_j pointing from the test mass to the closest point of approach is perpendicular to the velocity \vec{v} . The closest approach occurs at time t_j . As before, we express the result in terms of the Fourier amplitude $x_j(\Omega)$ of test-mass displacement,

$$x_j(\Omega) = \frac{2Gm}{v^2\Omega} (K_1(r_j\Omega/v) \cos(\alpha) + iK_0(r_j\Omega/v) \cos(\beta)) e^{i\Omega t_j}. \quad (5)$$

Here, m is the mass of the moving object, α is the angle between \vec{r}_j and the arm, β is the angle between \vec{v} and the

arm, and $K_n(x)$ is the modified Bessel function of the second kind. In all relevant cases, the argument $x = r_j \Omega / v$ obeys $x \gg |n^2 - 1/4|$ so that the modified Bessel functions can be expanded according to

$$K_n(x) \approx \sqrt{\frac{\pi}{2x}} e^{-x} \left(1 + \frac{4n^2 - 1}{8x} + \dots \right). \quad (6)$$

The moving object could be a car, a person, or a quasistatic density fluctuation in the atmosphere localized within a cell and transported by wind. In this last case, one would consider a spatial distribution of many cells with typical quasistatic density perturbation and volume determined by a spatial correlation function [51].

In fact, one motivation to build low-frequency detectors underground comes from this type of gravity perturbation. Evaluating a few examples, one finds that the associated NN would completely dominate the signal if it was not for the exponential suppression in Eq. (6), which is effective especially for underground detectors. The threshold frequency f_0 above which NN from uniformly moving objects can be neglected is given by $f_0 \approx v/(2\pi r_j)$. At the surface, one could imagine constructing an environmental shield around test masses with a radius of about 10 m, so that typical threshold frequencies are close to 0.1 Hz almost independent of the object's mass m . So even an animal running at a straight line past the buildings of a surface detector could potentially generate significant NN up to the threshold frequency. Therefore, the only feasible solution to this problem is to build the detector several hundred meters underground and push f_0 below the detection band for all conceivable speeds v . As NN from an uncontrolled environment is avoided by increasing the distance between objects and test masses, NN control can in principle be achieved by enforcing a strict speed limit of all objects near test masses.

b. Newtonian noise from oscillating objects.— Isolated oscillating objects cannot exist as there must always be a reaction force on another object. For example, a shaking tree will transfer momentum to the ground generating seismic waves that are correlated with the motion of the tree. Therefore, the full problem of gravity perturbations from oscillating objects is difficult to analyze. The aim of this section is to provide NN estimates from the oscillating object itself without including reaction terms.

We will calculate the strain of the perturbation measured by two test masses at distance L to each other forming an interferometer arm in the direction of the unit vector \vec{n} . A point mass m is assumed to oscillate with amplitude $\vec{\xi}$ much smaller than its distance to the test masses. So we will always linearize the equations with respect to $\vec{\xi}$. Then the displacement of the first test mass has the well known dipole form

$$x_1 = -\frac{Gm}{r_0^3 \Omega^2} ((\vec{\xi} \cdot \vec{n}) - 3(\vec{e}_r \cdot \vec{n})(\vec{\xi} \cdot \vec{e}_r)), \quad (7)$$

where \vec{e}_r is the unit vector pointing from the first test mass to the object, and r_0 is the mean distance between them. The acceleration of the second test mass expressed in terms of the same unit vector \vec{e}_r reads

$$x_2 = -\frac{Gm}{r_0^3 \Omega^2} \frac{1}{(1 - 2\lambda(\vec{e}_r \cdot \vec{n}) + \lambda^2)^{5/2}} \cdot ((\vec{\xi} \cdot \vec{n}) - 3(\vec{e}_r \cdot \vec{n})(\vec{\xi} \cdot \vec{e}_r) + \lambda(3(\vec{\xi} \cdot \vec{e}_r) + (\vec{e}_r \cdot \vec{n})(\vec{\xi} \cdot \vec{n})) - 2\lambda^2(\vec{\xi} \cdot \vec{n})) \quad (8)$$

with $\lambda \equiv L/r_0$. We evaluate the strain for the case of an oscillating object at the surface directly above the first test mass that is located at a depth r_0 . In this case $\vec{e}_r \cdot \vec{n} \approx 0$ and the strain simplifies to

$$h = (x_2 - x_1)/L = -\frac{Gm}{r_0^3 \Omega^2 L} \left(\frac{(1 - 2\lambda^2)(\vec{\xi} \cdot \vec{n}) + 3\lambda(\vec{\xi} \cdot \vec{e}_r)}{(1 + \lambda^2)^{5/2}} - \vec{\xi} \cdot \vec{n} \right). \quad (9)$$

One can see that for small detectors with $\lambda \ll 1$, the strain in Eq. (9) is proportional to λ for vertical oscillations, or λ^2 for horizontal oscillations, which makes the strain disturbance independent of the distance L between the test masses or proportional to L . In the latter case we have the uncommon situation that strain noise increases with detector length.

We conclude this section with an estimate of NN from the sway of a single tree [62–64]. We assume that the tree crown displacement can be approximated as horizontal and that the test masses are located 1 km underground forming an interferometer arm of 20 m length. The natural frequency of a $h = 15$ m tall tree is about 0.4 Hz. We assume the stem diameter at breast height to be $\text{dbh} = 0.3$ m so that the parabolic estimate of its mass is about $m = \rho \pi / 2 (\text{dbh}/2)^2 h \approx 450$ kg with a density $\rho = 850$ kg/m³. Then the strain disturbance as the time-domain amplitude is given by

$$h = \frac{9G(m/2)}{2r_0^5 \Omega^2} (\vec{\xi} \cdot \vec{n}) L \approx 10^{-22}, \quad (10)$$

assuming that effectively only half of the tree mass is displaced and that the displacement amplitude at the natural frequency is 0.5 m in the direction of the arm. This strain value seems sufficiently small, but gravity perturbations from multiple trees could potentially add coherently.

c. Newtonian noise from fault rupture.— Teleseismic events can cause an immediate gravity perturbation in low-frequency GW detectors in addition to a delayed perturbation from seismic waves generated by these events that pass the detector. Between 10 mHz and 1 Hz, earthquakes and major explosions such as the eruption of volcanoes are examples of sources of strong gravity perturbations. Here we are interested in fault ruptures since the

rate of events with a significant magnitude can be very high in certain regions.

The prompt gravity perturbation from fault rupture can in principle include several distinct transients associated with lasting density changes near the fault that are built up during the fault rupture, compressional waves generated by the event, and also contributions from strong surface displacement at the epicenter depending on the event depth. The relative strength of these transients depends significantly on the location and orientation of the GW detector with respect to the fault plane. Details will be presented in an upcoming publication. Here we will focus on a simple estimate of the fault-rupture detection horizon of MANGO based on the well known lasting gravity change produced by earthquakes [65,66] that has been observed in multiple occasions [67,68].

The measured gravity strain depends on the location of the detector with respect to the fault and slip orientation. For a strike-slip event at 1000 km distance, with fault length and width equal to 12 km, the center of the fault at 25 km depth, slip size of 1 m, and ideal detector location, we obtain a lasting change in radial gravity strain of 4×10^{-18} . Rupturing a fault of this size would take about 2 s, which corresponds approximately to a magnitude $M = 6$ earthquake. As the event corner frequency would be about 0.5 Hz, this perturbation could easily be seen in the data. Similar results are obtained for dip-slip events and arbitrary fault orientations.

C. Newtonian noise subtraction

Since terrestrial gravity perturbations cannot be fully avoided, alternative noise-mitigation strategies need to be developed. One idea is to monitor the density fluctuations around the test masses. Most importantly, this means to measure seismic waves and atmospheric infrasound by means of sensor arrays. The sensor data can then be used to produce a coherent subtraction filter for NN (i.e. a Wiener or adaptive filter [69,70]). This technique seems to be very attractive since clearly a high number of sensors like seismometers and infrasound microphones should make it possible to subtract a large part of the NN. However, as we will demonstrate in this section, it is uncertain whether sufficiently sensitive seismic and infrasound sensors can be provided.

Even though infrasound waves are the atmospheric analog of compressional body waves, it is not possible to achieve high infrasound NN subtraction with a single microphone as suggested for compressional waves in [55] using a single seismic strainmeter. The main reason is that microphones respond to infrasound waves independently of the direction of propagation, whereas seismometers measure ground displacement in certain directions. In addition, it is generally impossible to achieve significant broadband subtraction of Rayleigh seismic NN with a single seismic sensor, independent of the type of seismic sensor that is used [70].

Figure 9 shows that seismic and atmospheric NN would have to be reduced by large factors to achieve sensitivity goals with respect to NN. Performance of NN subtraction over a band of frequencies not only depends on the sensitivity of the auxiliary sensors, but also on the design of the sensor array. Here we will present results for the atmospheric and Rayleigh seismic NN subtraction using Wiener filters as outlined in [71]. In Fig. 10, the three curves represent relative subtraction residuals for three spiral arrays. The calculation is based on an isotropic field of Rayleigh waves. The sensors measure vertical ground displacement with $\text{SNR} = 1000$. The detector length is $L = 200$ m. Array density determines the highest frequency up to which NN can be subtracted. At low frequencies, subtraction performance declines, because a larger fraction of the seismic signal leads to common-mode gravity perturbations that are rejected by the interferometer, and also because the array cannot provide reliable information about seismic waves that are much longer than the diameter of the seismic array (each contributing a $1/f$ at low frequencies). Therefore enlarging the array (without decreasing sensor density in the central part) would increase subtraction performance at the expense of deploying a much larger number of sensors. The same calculation is repeated for the infrasound NN for an infrasound field isotropic over a half space. The results are shown in Fig. 11. Even though the microphones are assumed to have the same sensitivity to pressure fluctuations as the seismic sensors to ground displacement, less subtraction is achieved. The reason is that NN from sound waves propagating in three dimensions is subtracted using a two-dimensional microphone array deployed on the Earth's surface. If it were possible to monitor atmospheric infrasound at different altitudes, then subtraction residuals could be similar to the seismic case. In summary, the results shown in Figs. 10 and 11 demonstrate

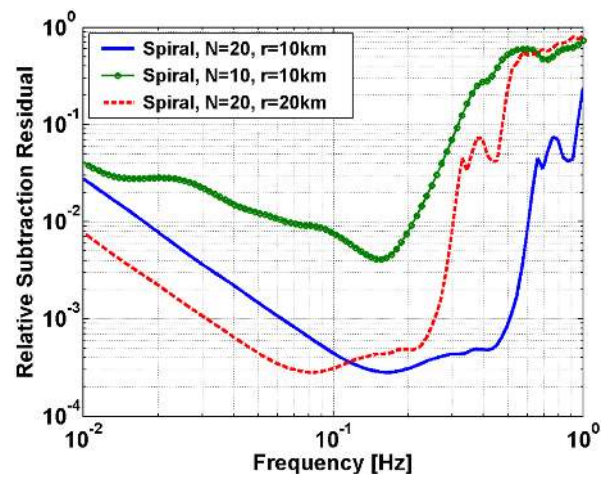


FIG. 10 (color online). Residuals of Rayleigh-wave gradient NN subtraction for double-wound spiral arrays using seismometers with $\text{SNR} = 1000$. Results are presented for different numbers N of seismometers and different array radii r .

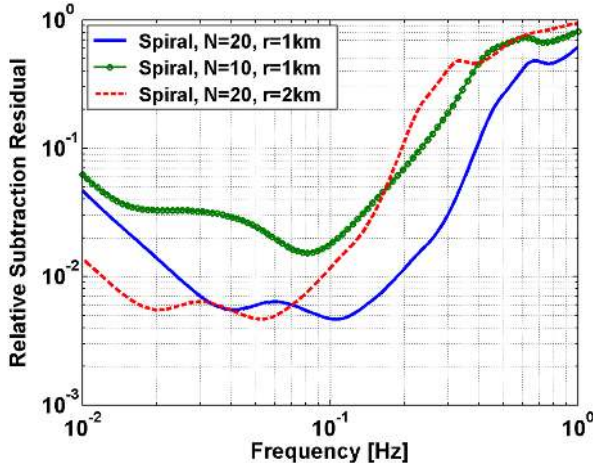


FIG. 11 (color online). Residuals of infrasound gradient NN subtraction for double-wound spiral arrays using microphones with $\text{SNR} = 1000$. Results are presented for different numbers N of microphones and different array radii r .

that it will be very challenging to achieve sufficient NN subtraction. A suppression of the NN by about 4 or 5 orders of magnitude at 0.1 Hz would be needed to make it comparable to the instrument noise limit. To achieve the goal, a larger number of more sensitive sensors will be required, and the arrays should ideally be tailored to the required NN subtraction factors.

We conclude this part with a brief discussion about the sensors required to achieve the NN subtraction goals. Subtraction of NN below instrumental noise requires the development of new environmental sensors, beyond the current needs in typical applications of seismometers and microphones. The sensitivities of various seismometers were compared in [35]. For example, a factor >10 improvement in seismometer sensitivity is required at 0.1 Hz with respect to the sensitivity of the best commercial sensors. Also, the best gravimeters (when used as seismometers) barely resolve the global new low-noise model [59] at frequencies above 10 mHz [72–74], but it is not completely understood what types of noise or environmental couplings are causing sensitivity limits in modern instruments. There are efforts to improve the low-frequency sensitivity of seismometers, and if for example the dominant noise is a result of coupling to the environment, like pressure or temperature changes, then coherent noise subtraction using additional thermometers or barometers could be a solution. Therefore, it is very important to investigate noise in seismometers and gravimeters; otherwise the GW band below 0.1 Hz may remain inaccessible to ground-based detectors. However, as such improvements do not meet fundamental limitations, NN subtraction is proposed as a potential solution in MANGO detectors. The situation is similar for infrasound microphones. However, high-sensitivity measurements of sound require additional techniques to reduce the influence from local pressure fluctuations produced by wind [75].

It has often been proposed to use additional laser interferometers to measure and subtract NN, but these schemes fail since laser interferometers are exclusively sensitive to gravity strains, and it would be impossible to distinguish NN from GWs. Instead, a possible solution would be to sense a degree of freedom of the gravity field that does not have contributions from GWs, but that shows correlations with the strain field with respect to terrestrial perturbations.

VI. SOURCES OF GRAVITATIONAL WAVES FROM 0.01 HZ TO 1 HZ

In this section we reevaluate commonly studied low-frequency sources in the context of MANGO GW detection. As for most GW detectors, the science case developed here is strongly supported by the likely contribution of binary compact objects, but a wider range of less likely sources is included illustrating that research on low-frequency signals is ongoing, and significant changes in detection probabilities are possible. The most likely rate estimates for compact-binary signals are employed as can be found for example in [76].

A. Compact binaries

In the following, we discuss the most well-understood gravitational-wave sources for MANGO, namely compact binaries of white dwarfs, neutrons stars, and black holes. We will first briefly review the evolution of these binaries under gravitational radiation reaction, and then discuss several scenarios in which gravitational waves from these binaries might be detected.

1. Evolution of a compact binary under radiation reaction

Let us first briefly review the basics of gravitational waves from binaries in circular orbits (or *circular binaries*, which is probably a good approximation in most cases in this frequency range). This involves both the strain amplitude at a given frequency and the time spent at that frequency, as these both play a role in detectability. From Schutz [77], the angle-averaged strain amplitude measured a distance r from a circular binary of masses m_1 and m_2 (and hence total mass $M \equiv m_1 + m_2$ and symmetric mass ratio $\eta \equiv m_1 m_2 / M^2$) with a binary orbital frequency f_{bin} (and hence gravitational wave frequency $f_{\text{GW}} = 2f_{\text{bin}}$) is

$$h = \frac{2(4\pi)^{1/3}}{c^4} \frac{\eta(GM)^{5/3}}{r} f_{\text{GW}}^{2/3} \\ = 2.4 \times 10^{-22} \left[\frac{f_{\text{GW}}}{0.01 \text{ Hz}} \right]^{\frac{2}{3}} \frac{\eta}{0.25} \left[\frac{M}{2M_{\odot}} \right]^{\frac{5}{3}} \frac{10 \text{ kpc}}{r}, \quad (11)$$

where in the second line we normalize to an equal-mass binary ($\eta = 0.25$). Note that for comparable-mass sources, η is close to 0.25; for example, $m_1/m_2 = 1.5$ gives $\eta = 0.24$ and even $m_1/m_2 = 2$ gives $\eta = 2/9$, which is only an 11% change from 0.25.

From Peters [78] the semimajor axis a of a circular binary evolves adiabatically via gravitational radiation as

$$\dot{a} = -\frac{64}{5c^5} \frac{\eta(GM)^3}{a^3}. \quad (12)$$

Switching variables to $f_{\text{GW}} = (GM/a^3)^{1/2}/\pi$ gives

$$\dot{f}_{\text{GW}} = \frac{96\pi^{8/3}}{5c^5} \eta(GM)^{5/3} f_{\text{GW}}^{11/3}. \quad (13)$$

From \dot{f}_{GW} , we can estimate a characteristic time for radiation reaction,

$$T \equiv f_{\text{GW}}/\dot{f}_{\text{GW}}. \quad (14)$$

If f_{GW} is at least a factor of a few less than the merger frequency, then the time left before merger, or the additional lifetime of the inspiral, is

$$\begin{aligned} T_{\text{insp}} &= \frac{3}{8}T = \frac{5}{256\pi^{8/3}} \frac{c^5}{\eta(GM)^{5/3}} f_{\text{GW}}^{-8/3} \\ &= 5.5 \times 10^3 \text{ yr} \left[\frac{0.25}{\eta} \right] \left[\frac{M}{2M_\odot} \right]^{-5/3} \left[\frac{f_{\text{GW}}}{0.01 \text{ Hz}} \right]^{-8/3}. \end{aligned} \quad (15)$$

Suppose our detector has a noise spectral density of S_h . Then the signal-to-noise ratio, using the matched-filtering detection technique, is

$$\rho^2 = 4 \int_0^{+\infty} df \frac{|\tilde{h}(f)|^2}{S_h(f)}. \quad (16)$$

If the detector's spectral density and the amplitude of the GW are both roughly constant, then (as can also be seen using Parseval's theorem)

$$\rho^2 \approx \frac{4h^2T}{S_h}. \quad (17)$$

If ρ_* is the threshold for detectability, then for any GW signal h the detector's maximum spectral density is given by

$$S_* = \frac{4}{\rho_*^2} h^2 \min(T_{\text{insp}}, T_{\text{obs}}). \quad (18)$$

Here we have taken the minimum of the inspiral time T_{insp} and the observation time T_{obs} .

2. Individual neutron-star binaries

From Eq. (15), we see that for white dwarf and neutron star binaries below $f_{\text{GW}} \sim 0.1$ Hz, the inspiral time is greater than $\sim 10^7$ s, which we use as a fiducial observation time for MANGO. It is a conservative estimate taking into account that low-frequency ground-based detectors could frequently be perturbed by seismic or atmospheric events, either by direct vibrational disturbance or via gravitational coupling. Hence for those sources 10^7 s is the relevant time in Eq. (18). For more massive sources, such as IMBH-IMBH binaries, the inspiral time is relevant because it is shorter than 10^7 s. As a consequence, the IMBH spectrum in Fig. 12 falls as $f^{-2/3}$. Assuming a distance of 10 kpc for

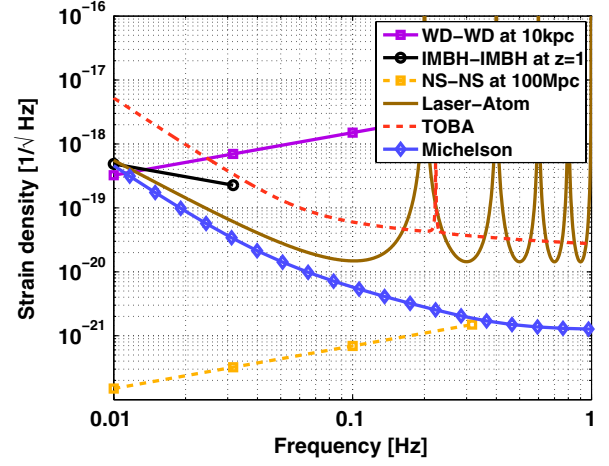


FIG. 12 (color online). Example tracks with residence-time-weighted spectral density for a double white dwarf merger at 10 kpc (solid red line; both have a mass of $0.6M_\odot$), a double neutron star merger at 100 Mpc (black dotted line; both have a mass of $1.5M_\odot$), and a double intermediate-mass black hole merger at $z = 1$ (blue dashed line; both have a mass of 10^4M_\odot). The IMBH-IMBH curve is terminated at the innermost stable circular orbit frequency as we see it in our frame (0.1 Hz).

WD binaries, 100 Mpc for NS binaries, and $z = 1$ for IMBH binaries, and assuming $\rho_*^2 = 4$, we plot in Fig. 12 the minimum spectrum for the detector at different frequencies.

To estimate the relevant distance for each type of binary event, we have to use our knowledge about their rates. Suppose the rate per Milky-Way equivalent galaxy (MWEG) is $\mathcal{R}_{\text{MWEG}}$. Then for a frequency f_{GW} and a corresponding lifetime of T_{insp} , the probability that there is at least one such binary in a MWEG is

$$p = 1 - \exp(-\mathcal{R}_{\text{MWEG}}T_{\text{insp}}) \approx \mathcal{R}_{\text{MWEG}}T_{\text{insp}}, \quad (19)$$

where in the last expression we assume $\mathcal{R}_{\text{MWEG}}T_{\text{insp}} \ll 1$.

For two neutron stars of $1.4M_\odot$, and assuming a galaxy rate from 1 to 1000 Myr^{-1} [76], we have a probability, ranging from 0.4% to 98%, to have at least one binary neutron star with a gravitational-wave frequency at or above 0.01 Hz. For the most likely rate of 100 Myr^{-1} , that probability becomes 34%. From Fig. 12, it is plausible for MANGO to reach 10 kpc, and therefore the chance for MANGO to detect a neutron star binary in our Galaxy is non-negligible.

One has to reach substantially farther in order to detect binaries from other galaxies. In the most pessimistic case, we will have to reach ~ 700 MWEG in order to guarantee a binary with 95% confidence, which implies a horizon distance of 56 Mpc. If we use the most likely rate, then to guarantee the same likelihood of detection we need to reach around 7.2 MWEGs, which is achievable if we can reach a horizon distance of ~ 5 Mpc. Here we have used the conversion formula of

$$N_G = \frac{4}{3} \pi \left(\frac{D_{\text{horizon}}}{\text{Mpc}} \right)^3 (2.26)^{-3} 0.0116, \quad (20)$$

which is Eq. (4) of Ref. [76] when D_{horizon} is larger than ~ 30 Mpc, and Fig. 1 of the same paper for smaller distances. Here, $1/2.26$ is the correction factor included to average over all sky locations and orientations, and 0.0116 Mpc^{-3} is the extrapolated density of MWEs in the Universe. Noting that D in Eq. (18) is the distance reachable by a detector after averaging, instead of the horizon distance, with a conversion factor of

$$D = \frac{D_{\text{horizon}}}{2.26}. \quad (21)$$

This means, at the most likely rate, we need $D \approx 2.2$ Mpc, while in the least rate, we need $D \approx 25$ Mpc. If we account for additional integration time, then from Fig. 12, it is plausible that MANGO can detect a NS binary from nearby galaxies.

The rate per galaxy of BH-NS and stellar-mass BH-BH mergers is less than for NS-NS, and the binaries are more massive and thus spend less time above 0.01 Hz, so it is highly unlikely that such binaries are in the MANGO band in the Galaxy at the moment. For example, the expected detection rate of stellar-mass BH binaries is about 1 yr^{-1} only for a very optimistic merger rate of $30 \text{ Myr}^{-1} \text{ MWE}^{-1}$. Such high rates have been obtained in [79], but the rate prediction would be about 2 orders of magnitude lower using rate estimates currently considered as likely [76]. Given that even the existence of intermediate-mass black holes is still under debate, estimates of their rates are even less certain. However, if multiple IMBHs can form in a dense stellar cluster (e.g., Gürkan *et al.* [80]) or separate clusters with IMBHs merge (e.g., Amaro-Seoane and Freitag [81], Amaro-Seoane *et al.* [82]), then depending on the fraction of clusters that form IMBHs and their masses and merger efficiencies there could be tens of mergers per year visible out to the $z \sim 1$ range of MANGO (Fregeau *et al.* [83], Mandel *et al.* [84], and Gair *et al.* [85]).

3. Individual white-dwarf binaries

Let us estimate the galactic merger rate of WD binaries. Collisions between two white dwarfs with a combined mass greater than the $\sim 1.4 M_{\odot}$ Chandrasekhar mass are candidates for Type Ia supernovae, and even collisions between two typical white dwarfs of mass $0.6 M_{\odot}$ release $\sim 10^{50}$ erg in gravitational binding energy, so we would expect them to be easily detectable. Thus a rate that implies such occurrences in our Galaxy more than once every few years is not plausible; we would have seen them. We note, however, that for two $0.6 M_{\odot}$ white dwarfs the inspiral time from 0.01 Hz is $T_{\text{insp}} \sim 2 \times 10^4$ yr, so if there are currently a few hundred such binaries in the Galaxy their merger rate would be only one per a few decades (note that the

expected number of binaries is $N = \mathcal{R} T_{\text{insp}}$), which could have been missed or misidentified. If there are supposed to be a few thousand, however, the rates get too high to miss. In other words, such a rough estimate puts

$$\mathcal{R}_{\text{WD}} \lesssim 10^{-2}/\text{yr}, \quad N \lesssim 10^2. \quad (22)$$

Other considerations lead to more concrete estimates. For example, from observations of WD binaries, Badenes and Maoz [86] estimate that in our Galaxy, the merger rate of super Chandrasekhar WD binaries (i.e. those with a total mass greater than the Chandrasekhar mass) is $\sim 6.4 \times 10^{-4}/\text{yr}$, and the total rate is $\sim 8 \times 10^{-3}/\text{yr}$. For a Chandrasekhar WD binary, its inspiral time at 0.01 Hz is 1.5×10^4 yr. Noting that the lifetime at a fixed frequency increases with a decreasing total mass, we can estimate that

$$N_{M > 1.4 M_{\odot}} \sim 10, \quad N_{M < 1.4 M_{\odot}} \sim 100. \quad (23)$$

This is compatible with the rough estimate above and suggests that a MANGO-like detector would have tens of sources in band. The lowest-period known WD/Wd binary is HM Cnc with a corresponding GW frequency of 6 mHz [87]. Therefore, all known binaries lie below the MANGO band.

4. Stochastic background from galactic and extragalactic binaries

If a large population of binaries with unknown parameters is viewed collectively as a source, the gravitational waves it emits may be viewed as a “stochastic background” [88,89]. However, in some cases, one can estimate parameters of some of the (stronger) binaries, and “resolve” part of this “stochastic background” into a complex but deterministic waveform [90,91].

Our ability to estimate parameters of the binary depends on two factors: (i) the duration of the observation and the individual waves and (ii) the sensitivity of our detector. Let us try to understand this for the simplest case in which all binary waves are quasimonochromatic but with a finite lifetime τ_* . Let us first select a finite subpopulation that already contributes to most of the spectrum; for example, a large enough finite cutoff distance. In this case, we first require (i) the lifetime of each wave τ_* and the observation time T_{obs} must both be long enough, so that within each frequency bin with a bandwidth of $2/\min(\tau_*, T_{\text{obs}})$, there is *at most one* binary of the subpopulation; we then require that (ii) in those bins with a binary, our detector have high enough sensitivity to detect the wave emitted by the binary.

As discussed by Farmer and Phinney [92], for a one-year observation, the galactic population of WD-WD binaries above 0.01 Hz (in the MANGO band) are all individually resolvable. On the other hand, the number of all extragalactic binaries is larger by a factor equal to the number of MWEs in the Universe, i.e. 10^{10} or more, and hence forms a population that is only individually resolvable at frequencies too high for most white dwarfs to reach, i.e.

above ~ 0.1 Hz, giving rise to a stochastic background below 0.1 Hz (see their Fig. 17). Farmer and Phinney [92] also give their expected extragalactic WD-WD background strength in their Fig. 16. They express it as $\Omega_{\text{gw}}(f)$, which is the energy density in a frequency band of width f centered on f , expressed as a fraction of the critical energy density for the Universe. From Eq. (5) of Phinney [93], the characteristic strain amplitude is related to $\Omega_{\text{gw}}(f)$ by

$$h_c(f) = [4G\rho_c\Omega_{\text{gw}}(f)/f^2]^{1/2} \\ \approx 1.6 \times 10^{-22} (\Omega_{\text{gw}}/10^{-12})^{1/2} (0.01 \text{ Hz}/f_{\text{GW}}), \quad (24)$$

where in the second line we have substituted $\rho_c = 9.5 \times 10^{-30} \text{ g cm}^{-3}$ (valid for a Hubble constant $H_0 = 71 \text{ km s}^{-1} \text{ Mpc}^{-1}$). On the other hand, using two colocated detectors with noise spectral density S_h , the characteristic h one can detect, after a duration of T_{obs} , is

$$h_c^*(f) \approx (2\pi f T_{\text{obs}})^{1/4} \sqrt{f S_h(f)} \\ \approx 2 \times 10^{-22} \left[\frac{S_h^{1/2}(f)}{10^{-19} \text{ Hz}^{-1/2}} \right] \left[\frac{f}{0.01 \text{ Hz}} \right]^{3/4} \left[\frac{T}{10^8 \text{ s}} \right]^{1/4}. \quad (25)$$

Note that when there are many sources, we can integrate over the entire observation time of 10^7 – 10^8 s without regard to how long each individual source takes to spiral in.

Figure 16 of Farmer and Phinney [92] suggests that Ω_{gw} may peak at $\sim 10^{-11}$ around 0.01 Hz. According to Eqs. (24) and (25), this background could be detectable with a 10^8 s MANGO integration but not likely with 10^7 . Above 0.01 Hz the expected background becomes progressively more uncertain, but possibilities exist up to ~ 0.1 Hz (after which the number of sources falls rapidly).

In comparison, the stochastic background from other extragalactic binaries (e.g., NSNS) are much less in magnitude and will be buried under the background arising from extragalactic WD binaries.

B. Helioseismic and other pulsation modes

Given that the Sun is extremely close and has strong helioseismic p modes at around ~ 300 s [94], one might hope that gravitational radiation from these modes could be seen with MANGO. Also the solar g modes, which have not been definitively detected yet, could potentially be observed. Their periods are all greater than about 45 min so that the detector would lie in the near-zone gravitational field [95].

Cutler and Lindblom [96] address this exact problem for LISA (which is more sensitive than MANGO at the relevant frequencies) and conclude that unless there are orders of magnitude more energy in the modes than expected, they will not be detectable even at 1 AU. This allows us to conclude that, unless other stars (particularly M dwarfs, whose general frequencies should be higher than those of

the Sun) have vastly greater energy in the modes than the Sun does, the cumulative gravitational wave background from their pulsations is much less than the amplitude from the Sun. This is for the same reason that the Sun has a larger optical flux than all other stars combined; the gravitational wave energy will add incoherently. Thus stellar pulsations will not be detectable.

C. Supernovae

In a recent paper on the preexplosive properties of the Type Ia supernovae, a GW emission mechanism was proposed occurring during the final accretion phase of a WD in a binary system [97]. The GW frequencies between 0.1 Hz and 0.5 Hz fall into the MANGO band with predicted strain amplitudes of up to $h = 10^{-19}$, which could easily be detected.

In contrast, it is very unlikely that GW emission from core-collapse supernovae would be detected with MANGO. However, computational models of supernovae are not converged yet, and each improvement in numerical technology (three-dimensional, fully general relativistic, better neutrino transport, inclusion of rotation, etc.) has brought surprises [98]. It is expected that most of the gravitational wave power will be at frequencies > 100 Hz (see, e.g., Fig. 4 of Ott [99]). Thus these are not likely to be detectable < 1 Hz gravitational wave sources even if a supernova happened in our Galaxy, but we should keep an open mind; given that simulations cannot be run for many seconds, perhaps there are unsuspected modes at a few tenths of a hertz.

D. Primordial stochastic background

It has been argued that the most important gravitational wave detection would be one from the very early universe (e.g., from the inflationary era) because this would give us information from an otherwise highly opaque epoch. Primordial stochastic backgrounds are predicted among others by inflationary, pre-big-bang and cosmic string models [100]. In standard inflationary models, however, the strength of this signal is tiny. From, e.g., Fig. 3 of Buonanno [101] one finds that Ω_{GW} from the inflationary gravitational wave background is likely to be less than $\sim 10^{-15}$, which is not only far below what MANGO could detect, but as we discussed earlier it will be completely masked by the unresolvable extragalactic WD-WD foreground up to ~ 0.1 Hz. It has been suggested that the ~ 0.1 Hz and above region will be “clean” in the sense that all foreground (i.e. redshifts in the single digits) sources will be individually resolvable; hence any sufficiently sensitive instrument might detect the inflationary background [90]. This presupposes, however, that the foreground sources can be subtracted with extreme fidelity, on the order of a part per thousand or possibly much better. Thus this seems unlikely. There is always the possibility of a surprise source in just the right frequency band, and big bang

nucleosynthetic constraints are only on the order of $\Omega_{\text{GW}} < 10^{-5}$ so a detectable stochastic background is possible, but it is not a probable source. The most sensitive searches of stochastic backgrounds require a network of detectors to search for correlations between detectors. In general, these searches are based on the assumption that no other correlated effects occur. However, several possible environmental influences have been identified that could produce correlated noise in two detectors separated by a large distance such as the Schumann resonances [102]. It can be expected that this problem is more significant at lower frequencies, and a careful analysis should be carried out.

VII. CONCLUSIONS

We have described three potential detectors in the 0.1–10 Hz band which can be astrophysically interesting and which would be complementary to the audio frequency GW detectors (LIGO, GEO, Virgo, KAGRA, and ET) as well as the space-borne detectors such as eLISA and DECIGO. With infrastructure sizes ranging from a few tens of meters for the TOBA concept to a few hundred meters for the laser and laser-atom interferometer concepts, these detectors are small scale compared to current and planned ground-based and space-borne interferometric detectors. Small infrastructure would significantly facilitate underground construction, which is necessary for MANGO detectors.

The key to this possibility is that the strain sensitivity in this band can be orders of magnitude worse than in

the audio band, due to the fact that (i) the strain amplitudes are larger and (ii) that the sources are much longer lived.

So far, the best strain sensitivity at 0.1 Hz is $10^{-8}/\sqrt{\text{Hz}}$, achieved with a prototype TOBA [103]. Significant experimental challenges must be overcome in order to make any of these types of detectors a reality. However, the added astrophysics which can be done with these instruments demands that we take on the challenge.

ACKNOWLEDGMENTS

We thank S. Nissanke for helpful discussions about low-frequency GW sources. The research of Y. C. is supported by NSF Grant No. PHY-1068881 and CAREER Grant No. PHY-0956189, as well as the David and Barbara Groce Fund at Caltech. M. E. and R. X. A. are supported by the National Science Foundation under Grant No. PHY-0757058. The research of M. C. M. was supported in part by a grant from the Simons Foundation (Grant No. 230349). M. C. M. also thanks the Department of Physics and Astronomy at Johns Hopkins University for their hospitality during his sabbatical. B. S. acknowledges the support of the Australian Research Council. A part of this work was supported by JSPS KAKENHI Grant No. 90313197. This manuscript has the LIGO document No. LIGO-P1300100. The research of J. H. for this paper was carried out at Caltech. H. M. thanks the National Science Foundation, the National Aeronautics and Space Agency, and the David and Lucile Packard Foundation.

-
- [1] LIGO Scientific Collaboration, *Rep. Prog. Phys.* **72**, 076901 (2009).
 - [2] T. Accadia *et al.*, *Classical Quantum Gravity* **28**, 114002 (2011).
 - [3] H. Lück, C. Affeldt, J. Degallaix, A. Freise, H. Grote, M. Hewitson, S. Hild, J. Leong, M. Prijatelj, K. A. Strain, B. Willke, H. Wittel, and K. Danzmann, *J. Phys. Conf. Ser.* **228**, 012012 (2010).
 - [4] K. Somiya, *Classical Quantum Gravity* **29**, 124007 (2012).
 - [5] R. X. Adhikari, [arXiv:1305.5188](https://arxiv.org/abs/1305.5188).
 - [6] M. Punturo *et al.*, *Classical Quantum Gravity* **27**, 194002 (2010).
 - [7] LISA Science Team, eLISA homepage (2012), <http://www.elisa-ngo.org>.
 - [8] P. L. Bender, M. C. Begelman, and J. R. Gair, *Classical Quantum Gravity* **30**, 165017 (2013).
 - [9] M. Ando *et al.*, *Classical Quantum Gravity* **27**, 084010 (2010).
 - [10] E. S. Phinney *et al.*, NASA Mission Concept Study, 2003.
 - [11] P. Amaro-Seoane *et al.*, *Classical Quantum Gravity* **29**, 124016 (2012).
 - [12] P. R. Saulson, *Phys. Rev. D* **30**, 732 (1984).
 - [13] S. A. Hughes and K. S. Thorne, *Phys. Rev. D* **58**, 122002 (1998).
 - [14] N. Yu and M. Tinto, *Gen. Relativ. Gravit.* **43**, 1943 (2011).
 - [15] P. W. Graham, J. M. Hogan, M. A. Kasevich, and S. Rajendran, *Phys. Rev. Lett.* **110**, 171102 (2013).
 - [16] S. Dimopoulos, P. W. Graham, J. M. Hogan, and M. A. Kasevich, *Phys. Rev. D* **78**, 042003 (2008).
 - [17] S. Dimopoulos, P. W. Graham, J. M. Hogan, M. A. Kasevich, and S. Rajendran, *Phys. Rev. D* **78**, 122002 (2008).
 - [18] M. Hohensee, S.-Y. Lan, R. Houtz, C. Chan, B. Estey, G. Kim, P.-C. Kuan, and H. Müller, *Gen. Relativ. Gravit.* **43**, 1905 (2011).
 - [19] R. Abbott *et al.*, *Classical Quantum Gravity* **21**, S915 (2004).
 - [20] T. Accadia *et al.*, *J. Low Freq. Noise Vib. Active Contr.* **30**, 63 (2011).
 - [21] J. G. Baker and J. I. Thorpe, *Phys. Rev. Lett.* **108**, 211101 (2012).
 - [22] P. L. Bender, *Gen. Relativ. Gravit.* **44**, 337 (2011).
 - [23] J. M. Hogan *et al.*, *Gen. Relativ. Gravit.* **43**, 1953 (2011).
 - [24] J. W. Armstrong, F. B. Estabrook, and M. Tinto, *Astrophys. J.* **527**, 814 (1999).

- [25] T. Kessler, C. Hagemann, C. Grebing, T. Legero, U. Sterr, F. Riehle, M. Martin, L. Chen, and J. Ye, *Nat. Photonics* **6**, 687 (2012).
- [26] G.D. Cole, W. Zhang, M.J. Martin, J. Ye, and M. Aspelmeyer, [arXiv:1302.6489](#).
- [27] J.G. Bohnet, Z. Chen, J.M. Weiner, D. Meiser, M.J. Holland, and J.K. Thompson, *Nature (London)* **484**, 78 (2012).
- [28] G. Mueller, *Opt. Express* **13**, 7118 (2005).
- [29] P. Kwee, C. Bogan, K. Danzmann, M. Frede, H. Kim, P. King, J. Pödl, O. Puncken, R.L. Savage, F. Seifert, P. Wessels, L. Winkelmann, and B. Willke, *Opt. Express* **20**, 10617 (2012).
- [30] P. Treutlein, K.Y. Chung, and S. Chu, *Phys. Rev. A* **63**, 051401 (2001).
- [31] G.D. McDonald, C.C. Kuhn, S. Bennetts, J.E. Debs, K.S. Hardman, J.D. Close, and N.P. Robins, *Phys. Rev. A* **88**, 053620 (2013).
- [32] S.-W. Chiow, T. Kovachy, H.-C. Chien, and M.A. Kasevich, *Phys. Rev. Lett.* **107**, 130403 (2011).
- [33] M. Ando, K. Ishidoshiro, K. Yamamoto, K. Yagi, W. Kokuyama, K. Tsubono, and A. Takamori, *Phys. Rev. Lett.* **105**, 161101 (2010).
- [34] G. Cella, V. Sannibale, R. DeSalvo, S. Márka, and A. Takamori, *Nucl. Instrum. Methods Phys. Res., Sect. A* **540**, 502 (2005).
- [35] A.T. Ringler and C.R. Hutt, *Seismol. Res. Lett.* **81**, 972 (2010).
- [36] T.T. Fricke, N.D. Smith-Lefebvre, R. Abbott, R. Adhikari, K.L. Dooley, M. Evans, P. Fritschel, V.V. Frolov, K. Kawabe, J.S. Kissel, B.J.J. Slagmolen, and S.J. Waldman, *Classical Quantum Gravity* **29**, 065005 (2012).
- [37] P. Astone *et al.* (IGEC-2 Collaboration), *Phys. Rev. D* **76**, 102001 (2007).
- [38] Y. Aso, *Phys. Lett. A* **327**, 1(2004).
- [39] K. Numata and J. Camp, *Appl. Opt.* **47**, 6832 (2008).
- [40] F. Garoi, J. Winterflood, L. Ju, J. Jacob, and D. Blair, *Rev. Sci. Instrum.* **74**, 3487 (2003).
- [41] J. Winterflood, D. Blair, and B. Slagmolen, *Phys. Lett. A* **300**, 122 (2002).
- [42] M. Varvella, E. Calloni, L.D. Fiore, L. Milano, and N. Arnaud, *Astropart. Phys.* **21**, 325 (2004).
- [43] R.W.P. Drever, in *Dark Matter in Cosmology Quantum Measurements Experimental Gravitation*, edited by R. Ansari, Y. Giraud-Heraud, and J.T.T. Van (Editions Frontières, Gif-sur-Yvette, France, 1996), p. 375.
- [44] G.D. Hammond, A. Pulido-Paton, C.C. Speake, and C. Trenkel, *Rev. Sci. Instrum.* **75**, 955 (2004).
- [45] A. Giazotto, *Phys. Lett. A* **245**, 203 (1998).
- [46] D. McClelland, N. Mavalvala, Y. Chen, and R. Schnabel, *Laser Photonics Rev.* **5**, 677 (2011).
- [47] E.E. Mikhailov, K. Goda, T. Corbitt, and N. Mavalvala, *Phys. Rev. A* **73**, 053810 (2006).
- [48] M. Fleischhauer, A. Imamoglu, and J.P. Marangos, *Rev. Mod. Phys.* **77**, 633 (2005).
- [49] F. Vetrano and A. Viceré, *Eur. Phys. J. C* **73**, 2590 (2013).
- [50] M. Beccaria *et al.*, *Classical Quantum Gravity* **15**, 3339 (1998).
- [51] T. Creighton, *Classical Quantum Gravity* **25**, 125011 (2008).
- [52] S. Bonnefoy-Claudet, F. Cotton, and P.-Y. Bard, *Earth-Sci. Rev.* **79**, 205 (2006).
- [53] B. Kimball and E. Lemon, *J. Geophys. Res.* **75**, 6771 (1970).
- [54] M. Hedlin, K. Walker, D. Drob, and C. de Groot-Hedlin, *Annu. Rev. Earth Planet. Sci.* **40**, 327 (2012).
- [55] J. Harms, R. DeSalvo, S. Dorsher, and V. Mandic, [arXiv:0910.2774](#).
- [56] P. Bormann, B. Engdahl, and R. Kind, *New Manual of Seismological Observatory Practice* (GFZ, Potsdam, 2002), Chap. 2.
- [57] R.K. Cessaro, *Bull. Seismol. Soc. Am.* **84**, 142 (1994).
- [58] J. Harms *et al.*, *Classical Quantum Gravity* **27**, 225011 (2010).
- [59] J. Peterson, Open-file Report No. 93-322, 1993.
- [60] J.R. Bowman, G.E. Baker, and M. Bahavar, *Geophys. Res. Lett.* **32**, L09803 (2005).
- [61] K.S. Thorne and C.J. Winstein, *Phys. Rev. D* **60**, 082001 (1999).
- [62] T. Flesch and J. Wilson, *Agr. Forest Meteorol.* **93**, 229 (1999).
- [63] J. Wilson and T. Flesch, *Agr. Forest Meteorol.* **93**, 259 (1999).
- [64] T. Flesch and J. Wilson, *Agr. Forest Meteorol.* **93**, 243 (1999).
- [65] S. Okubo, *J. Geophys. Res.* **97**, 7137 (1992).
- [66] S. Okubo, *Geophys. J. Int.* **115**, 921 (1993).
- [67] Y. Imanishi, T. Sato, T. Higashi, W. Sun, and S. Okubo, *Science* **306**, 476 (2004).
- [68] G. Cambiotti and R. Sabadini, *J. Geophys. Res.* **118**, 1 (2013).
- [69] G. Cella, in *Recent Developments in General Relativity* (Springer, New York, 2000), pp. 495–503.
- [70] J.C. Driggers, J. Harms, and R. X. Adhikari, *Phys. Rev. D* **86**, 102001 (2012).
- [71] M. Beker *et al.*, *Gen. Relativ. Gravit.* **43**, 623 (2011).
- [72] J.M. Goodkind, *Rev. Sci. Instrum.* **70**, 4131 (1999).
- [73] D. Banka and D. Crossley, *Geophys. J. Int.* **139**, 87 (1999).
- [74] M. Freybourger, J. Hinderer, and J. Trampert, *Phys. Earth Planet. Inter.* **101**, 203 (1997).
- [75] R. Burridge, *Geophys. J. Int.* **26**, 53 (1971).
- [76] J. Abadie *et al.*, *Classical Quantum Gravity* **27**, 173001 (2010).
- [77] B.F. Schutz, in *Relativistic Gravitation and Gravitational Radiation*, edited by J.-A. Marck and J.-P. Lasota (Cambridge University Press, Cambridge, 1997), p. 447.
- [78] P.C. Peters, *Phys. Rev.* **136**, B1224 (1964).
- [79] K. Belczynski, M. Dominik, T. Bulik, R. O’Shaughnessy, C. Fryer, and D.E. Holz, *Astrophys. J. Lett.* **715**, L138 (2010).
- [80] M.A. Gürkan, J.M. Fregeau, and F.A. Rasio, *Astrophys. J. Lett.* **640**, L39 (2006).
- [81] P. Amaro-Seoane and M. Freitag, *Astrophys. J. Lett.* **653**, L53 (2006).
- [82] P. Amaro-Seoane, S. Konstantinidis, M.D. Freitag, M.C. Miller, and F.A. Rasio, [arXiv:1211.6738](#).
- [83] J.M. Fregeau, S.L. Larson, M.C. Miller, R. O’Shaughnessy, and F.A. Rasio, *Astrophys. J. Lett.* **646**, L135 (2006).
- [84] I. Mandel, D.A. Brown, J.R. Gair, and M.C. Miller, *Astrophys. J.* **681**, 1431 (2008).

- [85] J. R. Gair, I. Mandel, M. C. Miller, and M. Volonteri, *Gen. Relativ. Gravit.* **43**, 485 (2011).
- [86] C. Badenes and D. Maoz, *Astrophys. J. Lett.* **749**, L11 (2012).
- [87] G. H. A. Roelofs, A. Rau, T. R. Marsh, D. Steeghs, P. J. Groot, and G. Nelemans, *Astrophys. J. Lett.* **711**, L138 (2010).
- [88] T. Regimbau and V. Mandic, *Classical Quantum Gravity* **25**, 184018 (2008).
- [89] T. Regimbau, *Res. Astron. Astrophys.* **11**, 369 (2011).
- [90] C. Cutler and J. Harms, *Phys. Rev. D* **73**, 042001 (2006).
- [91] J. Harms, C. Mahrtdt, M. Otto, and M. Prieß, *Phys. Rev. D* **77**, 123010 (2008).
- [92] A. J. Farmer and E. S. Phinney, *Mon. Not. R. Astron. Soc.* **346**, 1197 (2003).
- [93] E. S. Phinney, [arXiv:astro-ph/0108028](https://arxiv.org/abs/astro-ph/0108028).
- [94] D. J. Thomson, L. J. Lanzerotti, F. L. Vernon, M. R. Lessard, and L. T. Smith, *Proc. IEEE* **95**, 1085 (2007).
- [95] T. Appourchaux *et al.*, *Astron. Astrophys. Rev.* **18**, 197 (2010).
- [96] C. Cutler and L. Lindblom, *Phys. Rev. D* **54**, 1287 (1996).
- [97] A. Tornambé and L. Piersanti, *Mon. Not. R. Astron. Soc.* **431**, 1812 (2013).
- [98] C. D. Ott, E. Abdikamalov, P. Mösta, R. Haas, S. Drasco, E. P. O'Connor, C. Reisswig, C. A. Meakin, and E. Schnetter, *Astrophys. J.* **768**, 115 (2013).
- [99] C. D. Ott, *Classical Quantum Gravity* **26**, 204015 (2009).
- [100] B. P. Abbott *et al.*, *Nature (London)* **460**, 990 (2009).
- [101] A. Buonanno, [arXiv:gr-qc/0303085](https://arxiv.org/abs/gr-qc/0303085).
- [102] E. Thrane, N. Christensen, and R. Schofield, *Phys. Rev. D* **87**, 123009 (2013).
- [103] K. Ishidoshiro, M. Ando, A. Takamori, H. Takahashi, K. Okada, N. Matsumoto, W. Kokuyama, N. Kanda, Y. Aso, and K. Tsubono, *Phys. Rev. Lett.* **106**, 161101 (2011).